CHEMISTRY
A EUROPEAN JOURNAL

ChemPubSoc Europe

DOI: 10.1002/chem.201202849

VIP

The Role of a Dipeptide Outer-Coordination Sphere on H_2-Production Catalysts: Influence on Catalytic Rates and Electron Transfer

Matthew L. Reback,[a] Bojana Ginovska-Pangovska,[a] Ming-Hsun Ho,[a] Avijita Jain,[b] Thomas C. Squier,[a] Simone Raugei,*[a] John A. S. Roberts,*[a] and Wendy J. Shaw*[a]

Abstract: The outer-coordination sphere of enzymes acts to fine-tune the active site reactivity and control catalytic rates, suggesting that incorporation of analogous structural elements into molecular catalysts may be necessary to achieve rates comparable to those observed in enzyme systems at low overpotentials. In this work, we evaluate the effect of an amino acid and dipeptide outer-coordination sphere on $[Ni(P^{Ph}_2N^{Ph\text{-}R}_2)_2]^{2+}$ hydrogen production catalysts. A series of 12 new complexes containing non-natural amino acids or dipeptides was prepared to test the effects of positioning, size, polarity and aromaticity on catalytic activity. The non-natural amino acid was either 3-(*meta*- or *para*-aminophenyl)propionic acid terminated as an acid, an ester or an amide. Dipeptides consisted of one of the non-natural amino acids coupled to one of four amino acid esters: alanine, serine, phenylalanine or tyrosine. All of the catalysts are active for hydrogen production, with rates averaging $\sim 1000\ s^{-1}$, 40% faster than the unmodified catalyst. Structure and polarity of the aliphatic or aromatic side chains of the C-terminal peptide do not strongly influence rates. However, the presence of an amide bond increases rates, suggesting a role for the amide in assisting catalysis. Overpotentials were lower with substituents at the *N*-phenyl *meta* position. This is consistent with slower electron transfer in the less compact, *para*-substituted complexes, as shown in digital simulations of catalyst cyclic voltammograms and computational modeling of the complexes. Combining the current results with insights from previous results, we propose a mechanism for the role of the amino acid and dipeptide based outer-coordination sphere in molecular hydrogen production catalysts.

Keywords: electrochemistry · homogeneous catalysis · hydrogen production · outer coordination sphere · peptide catalysts

Introduction

The protein scaffold or outer-coordination sphere of metalloenzymes plays a critical role in their resulting activity. Channels control the timed transport of electrons, substrates and products to and from the buried active site, and an environment is created around the active site that stabilizes ligands, influences redox potentials and controls the electric polarizability.[1] This environment can be achieved with sterics, hydrogen bonding, and/or by global effects such as the overall dielectric, the result of which creates a fine-tuned environment for achieving rates and efficiencies that are unmatched with synthetic analogs. Acidic, basic, polar and aromatic residues have all been implicated in modulating or tuning enzyme active sites.[1–2]

The importance of the environment created by the outer-coordination sphere has been demonstrated by DeGrado's group, who used artificial enzymes to show the stabilizing influence of outer-coordination sphere hydrogen bonds,[3] and in work by Lu's group, who have demonstrated the ability to tune redox potentials over a range of 700 mV with modest changes in the environment near the active site of a copper azurin protein.[4] The importance of the active site environment in enzyme catalysts suggests that controlling the environment around molecular catalysts may also provide significant benefit. This approach also has the potential to provide insight into the role of the enzymatic scaffold because molecular catalysts are likely to have fewer complications due to their comparative simplicity.

Hydrogenases are a class of enzymes of interest for their ability to efficiently and reversibly reduce H^+ to H_2.[5] A second-coordination sphere pendant amine has been identified from the crystal structure of the active site of [FeFe]-hydrogenase (**Ia**).[6] Studies of functional mimics have shown this to be essential for catalysis, and have led to catalysts that can meet (**Ib**) or exceed (**Ic**) the rates of the enzyme, but at higher overpotentials (300–600 mV).[7] These results suggest a pivotal role of the hydrogenase outer-coordination

[a] Dr. M. L. Reback, M. Sc. B. Ginovska-Pangovska, Dr. M.-H. Ho, Dr. T. C. Squier, Dr. S. Raugei, Dr. J. A. S. Roberts, Dr. W. J. Shaw
Pacific Northwest National Labs
Richland, WA 99354 (USA)
E-mail: wendy.shaw@pnnl.gov

[b] Dr. A. Jain
Current address:
Department of Chemistry
Indiana University of Pennsylvania
Indiana, PA 15705 (USA)

Supporting information for this article is available on the WWW under http://dx.doi.org/10.1002/chem.201202849.

sphere in achieving energy efficiency in producing hydrogen, but the influence of the outer-coordination sphere on these mimics has been largely unexplored.

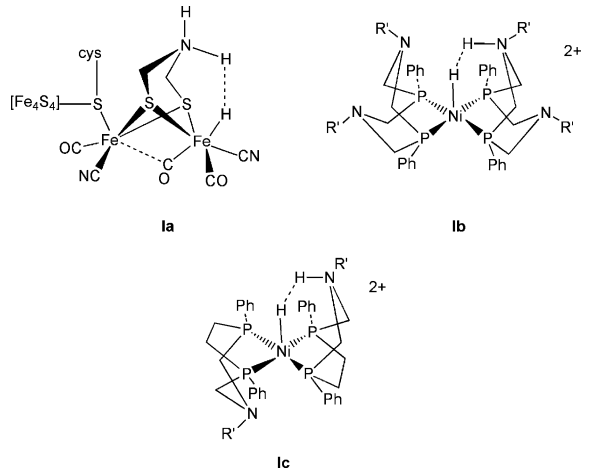

The environment around the active site of hydrogenase, along with many metalloenzymes, is highly polar and charged.[1,8] Within 9 Å of the bimetallic cluster in the active site of [NiFe]-hydrogenase, there are 60% acidic, basic or polar residues, compared to typical proteins which have a core consisting of 60% hydrophobic residues.[9] Although systematic mutations to test the role of the environment around the active site have not been explored, we have been studying the effect of outer-coordination sphere amino acids in molecular catalysts to determine if they can enhance catalysis, as well as provide insight into the enzyme. Initial investigations on the role of acidic and basic residues around functional mimics of hydrogenase (**Ib**), attached through a non-natural amino acid linker to generate dipeptide containing catalysts, $[Ni(P^{Ph}{}_2N^{Ph\text{-}dipeptide}{}_2)_2]^{2+}$, showed an order of magnitude variation in rates, as much as five times faster than the unmodified catalyst (**Ib**).[10] The enhancement in rates was thought to be due to an ability to concentrate protons around the active site, although a clear mechanism was not easily established.

This paper presents a series of functional hydrogenase mimics having the formula $[Ni(P^{Ph}{}_2N^{Ph\text{-}R}{}_2)_2]^{2+}$ (**IIa** and **IIb**, Figure 1), featuring a series of amino acid or dipeptide substituents at the *N*-phenyl rings attached at either the *meta*- or *para*- positions. The non-natural amino acid systems (3-(3-or 4-aminophenyl)propionic acid) are terminated as an acid, an ethyl ester or an amide. The dipeptide systems have an additional esterified amino acid residue coupled to the non-natural amino acid, including alanine ethyl ester (AlaOEt, with a methyl side chain at the central carbon), serine methyl ester (SerOMe, with a methoxy group at the central carbon), phenylalanine methyl ester (PheOMe, with a benzyl at the central carbon), or tyrosine methyl ester (TyrOMe, with a *para*-hydroxybenzyl at the central carbon). This set of complexes presents a matrix of comparisons: of the role of terminal functionality with the monopeptide complexes; of size effects with the amino acid versus dipeptide complexes; of the effects of aromaticity and polarity with the different esterified dipeptides; and of functional group positioning by comparison of *para*- and *meta*-substituted complexes. The comparisons are based on measurements of turnover frequency (TOF) at different potentials, voltammetric studies of the catalysts themselves, and complementary molecular dynamics (MD) studies. This paper addresses each of these comparisons to provide a mechanistic understanding of the role of the environment created by the outer-coordination sphere on molecular catalysts.

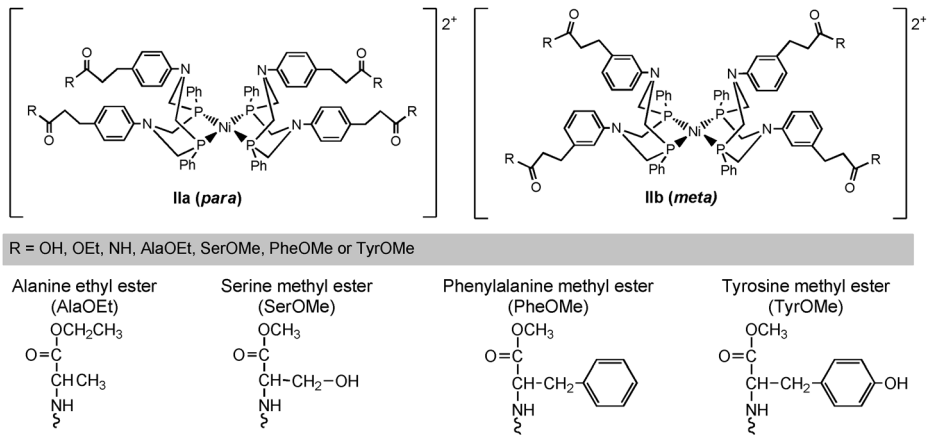

Figure 1. Amino acid and dipeptide complexes investigated in this study.

Results

Synthesis and characterization: Cyclic diphosphines containing the non-natural amino acid residues 3-(*meta*- or *para*-aminophenyl)propionic acid were prepared with an amide ($P^{Ph}{}_2N^{m/pNN\text{-}NH_2}{}_2$), ethyl ester ($P^{Ph}{}_2N^{m/pNN\text{-}OEt}{}_2$), or carboxylic acid termination ($P^{Ph}{}_2N^{m/pNNA}{}_2$), following previously described protocols.[10a] The dipeptide-functionalized $P^{Ph}{}_2N^{NNA\text{–}amino\ acid\ ester}{}_2$ ligands were prepared from $P^{Ph}{}_2N^{m/pNNA}{}_2$ by coupling the amino acid esters AlaOEt, SerOMe, PheOMe, or TyrOMe using standard TBTU/HOBT/DIPEA peptide coupling protocols, as shown in Scheme 1, reaction 1.[11] The ligands were isolated as off-white solids in low to moderate yields (20–60% for the dipeptides) and high purity, and were characterized using elemental analysis, $^{31}P\{^1H\}$, ^1H and ^1H-TOCSY NMR spectroscopy, affording data consistent with the proposed structures. Nickel complexes were pre-

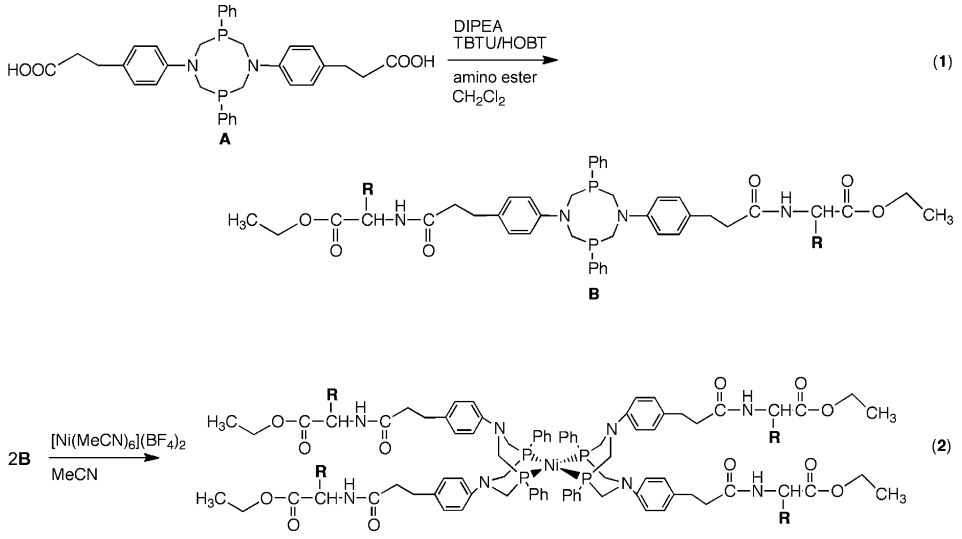

Scheme 1. Synthesis of the $P^{Ph}{}_2N^{NNA\text{–amino acid ester}}{}_2$ ligands (top). Synthesis of the $[Ni(P^{Ph}{}_2N^{NNA\text{–amino acid ester}}{}_2)_2]^{2+}$ complexes (bottom). R represents the amino acid side chain.

pared by reacting two equivalents of a $P^{Ph}{}_2N^{NNA\text{-amino acid ester}}{}_2$ ligand with one equivalent of $[Ni(MeCN)_6]^{2+}$ in acetonitrile, resulting in a red solution from which a moderately air sensitive metal complex was obtained in high yield (70–90%) and high purity, Scheme 1, reaction 2. The $[Ni(P^{Ph}{}_2N^{m/p\text{NNA-amino acid ester}}{}_2)_2)^{2+}$ complexes were characterized by $^{31}P\{^1H\}$, ^1H and ^1H-TOCSY NMR spectroscopy, mass spectrometry and electrochemistry, all of which are consistent with the proposed structures and similar to other reported complexes of this type.[5c,7b,c,10] Hereafter the nickel complexes are referred to by the position and identity of the amino acid or dipeptide substituent: for example *m*-NNA-SerOMe refers to the nickel complexes that are substituted off the phenyl ring in the *meta*-position and contain the non-natural amino acid coupled to serine methyl ester.

The $^{31}P\{^1H\}$ NMR spectra of the metal complexes all show a single phosphorous resonance between 4 and 6 ppm (Figure 2A), as previously reported.[10a] The ^{31}P resonances for the *meta*-substituted complexes (~4.6 ppm) are consistently shifted upfield as compared to the *para*-substituted complexes (~5.2 ppm), indicating increased electron density at the phosphorous atom, as expected (Table S1). The restricted exchange process observed for other dipeptide complexes of this type was not observed for the ester and amide complexes reported here.[10]

Two-dimensional ^1H-TOCSY spectra were used to assign the 1D-^1H NMR spectra (Figure 2B). In particular, the presence of the amide, identified by its coupling with the Cα proton of the amino acid ester, confirms that the added amino acid ester was coupled to the non-natural amino acid of the $P^{Ph}{}_2N^{NNA}{}_2$ ligand (Scheme 1). Comparing the integration of the amide protons to the Cα protons, as well as other protons in the ligand, confirms complete coupling. The amide-NH and Cα proton chemical shifts are reported in Table S1.

Electrochemical studies: Each of the dipeptide ester, amino acid ester and amino amide complexes reported in this study showed two distinct, reversible reduction waves assigned to the $Ni^{II/I}$ and the $Ni^{I/0}$ couples (Figure 3). Diffusion control was demonstrated by a linear increase in the non-catalytic current (i_p) with the square root of the scan rate ($v^{1/2}$) for the $Ni^{II/I}$ couple (Figure S1). The *meta*- and *para*-substituted non-natural amino acid complexes, *m*/*p*-NNA, show quasi-reversible $Ni^{II/I}$ and irreversible $Ni^{I/0}$ couples. Redox potentials ($E_{1/2}$), reported vs. the Cp_2Fe^+/Cp_2Fe couple at 0.0 V, and peak-to-peak separations (ΔE_p) are presented in Table S2.

The modifications to the outer-coordination sphere were specifically selected to minimize the impact on the electronics of the metal. Differences in redox potentials are small, as expected given the distance and number of bonds separating the structural modifications from the metal center. $E_{1/2}$ values are within 20 mV for both the $Ni^{II/I}$ potentials (−0.83

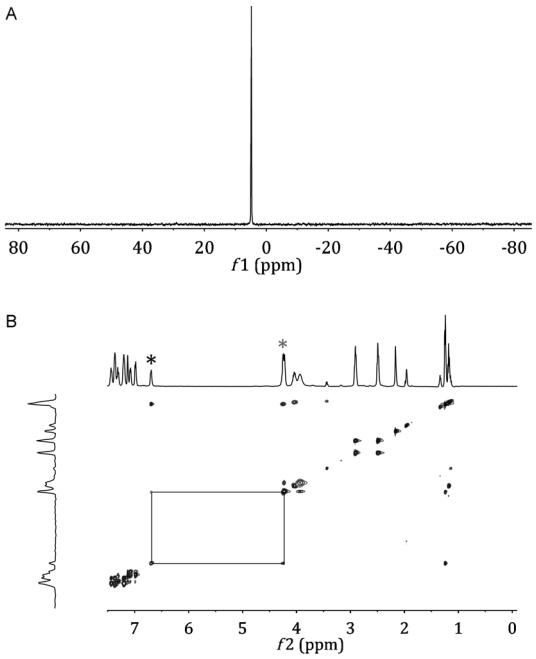

Figure 2. A) $^{31}P\{^1H\}$ spectrum of *m*-NN-OEt shown is representative of all of the nickel complexes reported in this paper. B) ^1H TOCSY was used to assign the ^1H NMR spectra (*m*-NNA-AlaOEt is shown). The presence of coupling between the amide resonance (dark asterisk) and the Cα resonance (light asterisk), shown by the solid lines, provided direct confirmation that the amino acid was coupled.

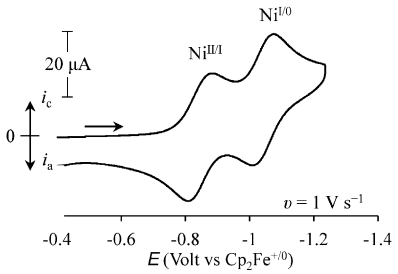

Figure 3. Cyclic voltammogram of *p*-NNA-AlaOEt (0.7 mM, scan rate v = 1 V s^{-1}) in acetonitrile (0.2 M $Et_4N^+BF_4^-$) showing reversible Ni$^{II/I}$ and Ni$^{I/0}$ redox couples typical of all the complexes reported with the exception of the *meta*- and *para*-non-natural acid complexes showing quasireversible Ni$^{II/I}$ couples.

to −0.85 V) and the Ni$^{I/0}$ potentials (−1.03 to −1.05 V). Potentials are uniformly more positive for the *meta*- versus *para*-substituted complexes, by 10 mV for the Ni$^{II/I}$ couples and by 20 mV for the Ni$^{I/0}$. Values of ΔE_p for the Ni$^{I/0}$ redox couples are between 60 and 66 mV, however, the ΔE_p values for the Ni$^{II/I}$ couples range from 63 to 120 mV (scan rate v = 1.0 V s^{-1}), and are generally larger for the *para*-substituted complexes. This reflects differences in electron transfer kinetics, as discussed in detail below.

Catalytic hydrogen production: All of the reported nickel complexes are active electrocatalysts for the production of H_2 (Table 1). Protonated dimethylformamide ($DMFH^+$, pK_a 6.1 in acetonitrile)[12] was added to acetonitrile solutions of each non-natural amino acid or dipeptide substituted nickel catalyst until the ratio of i_{cat}/i_p stopped increasing (the acid independent region,[5c, 7b, c, 10] requiring ~0.08 to 0.11 M acid for the catalyst concentrations employed, Figure S2). Figure 4 A and B show voltammograms recorded at acid independence for the *para*- and *meta*-substituted serine complexes, *p*-NNA-SerOMe and *m*-NNA-SerOMe, which are representative of the electrochemistry for each of the complexes. As has been reported previously,[7b, c, 10a] adding water in limited quantities increases the catalytic current until a new maximum is attained at water concentrations between 0.5 and 1.5 M (Figure 4 and Table 1). Catalytic cyclic voltammograms were collected at 1 V s^{-1}, in the scan rate independent region (Figure S3).

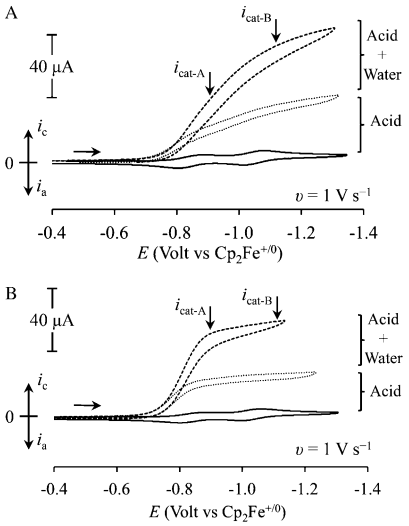

Figure 4. Addition of acid followed by the addition of water into a solution of A) *p*-NNA-SerOMe and B) *m*-NNA-SerOMe, results in an increase in current, indicative of catalytic activity. These results are typical for those observed for each of the catalysts.

Catalytic rates were determined at two potentials, i_{cat-A} and i_{cat-B}, as indicated with the arrows in Figure 4, due to the distinctly different shape of the catalytic wave for the *para*-substituted complexes. Catalytic currents either increased gradually (*para*-substituted complexes, Figure 4 A), or rapidly, leading to a plateau (*meta*-substituted complexes, Figure 4 B). Turnover frequencies were determined using equation 1 (Methods Section) and are reported in Table 1. At their fastest, all of these catalysts have similar TOF's, with an average of ~1000 s^{-1} at the larger applied potentials in the presence of both acid and water (Table 1, i_{cat-B}), ~40% faster than the fastest rate for the unmodified parent complex (having phenyl substituents at the P and N atoms).

The role of the amide functional group: While differences in catalytic rates are not large, an increase in rate for any complex with an amide bond is ob-

Table 1. Turnover frequencies (TOF, s^{-1}) for hydrogen production by [Ni($P^{Ph}_2N^{m/p\text{NNA-amino acid ester}}_2$)$_2$]$^{2+}$ at overpotentials of 300 and 400 mV, and the percent increase in rate between the overpotentials.

Metal complex	i_{cat-A} (−0.9 V) OP (~300 mV) TOF [s^{-1}] (±10%)	TOF with H_2O (±10%)	i_{cat-B} (−1.1 V) OP (~400 mV) TOF [s^{-1}] (±10%)	TOF with H_2O (±10%)	[%] increase in TOF vs OP w/ H_2O[a]
para					
p-NNA-TyrOMe	110	640	290	1200	87
p-NNA-AlaOEt	120	670	230	1100	64
p-NNA-SerOMe	110	600	210	1100	83
p-NN-NH_2	180	640	290	1030	60
p-NN-OEt[b]	177	700	250	950	35
p-NNA-PheOMe	90	440	200	910	107
p-NNA[b,c]	280	650	610	840	29
meta					
m-NNA-PheOMe	160	930	220	1180	27
m-NNA-SerOMe	160	880	190	1080	23
m-NN-NH_2	182	918	230	1100	20
m-NNA-AlaOEt	120	920	180	1040	13
m-NNA-TyrOMe	130	770	220	1040	35
m-NN-OEt	160	640	220	780	21
m-NNA[c]	500	560	670	790	41
[Ni($P^{Ph}_2N^{Ph}_2$)$_2$]$^{2+}$[d]	590	720	NA	NA	NA

[a] $((i_{cat-B}-i_{cat-A})/i_{cat-A}\times 100)$. [b] Data for these complexes were originally reported by Jain et al.[10a] The values reported in this paper were re-run under identical catalytic conditions used for the amino acid ester complexes for consistency. [c] These complexes showed quasi reversible II/I and I/0 couples and were run under slightly different conditions (see Experimental Section). [d] Data is taken from Kilgore et al.[7b]

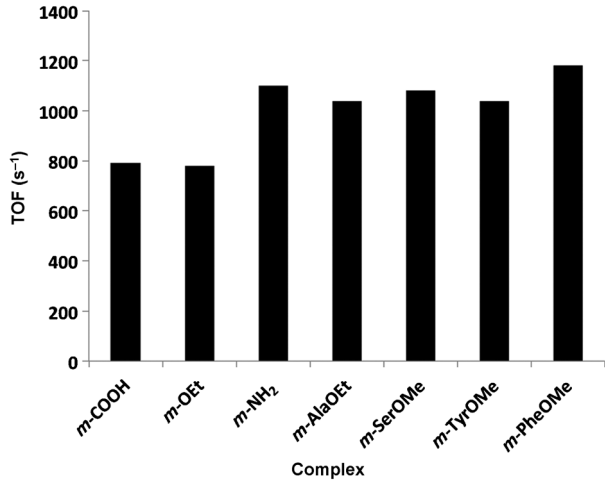

Figure 5. TOF values of the *meta*-substituted complexes are displayed as a function of amino acid or dipeptide substituent, showing a moderate but clear enhancement of the rate when an amide bond is present.

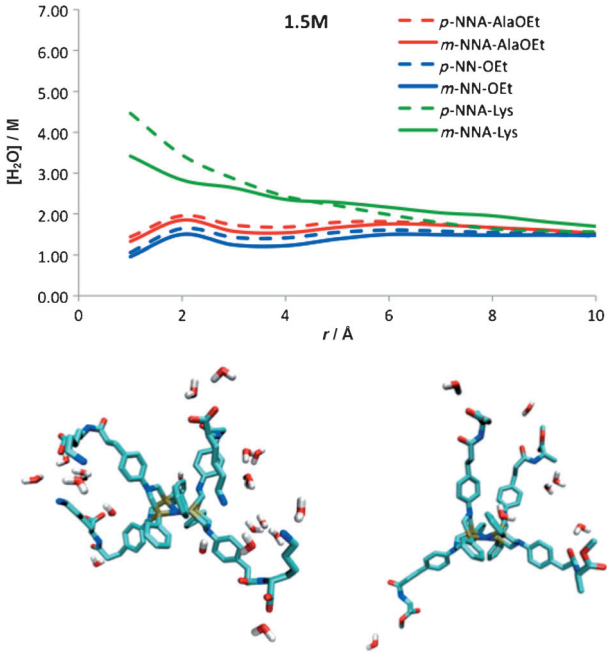

Figure 6. Concentration of water as a function of the distance from the solvent-accessible surface of the catalyst for a 1.5 M water solution in acetonitrile (top), and snapshots from the MD simulations showing the distribution of water within 3 Å of the complex for *p*-NNA-Lys (bottom left) and *p*-NNA-AlaOEt (bottom right). The *m*/*p*-NNA-Lys concentrates significantly more water near the surface of the molecule than the amide containing *p*-NNA-AlaOEt or the ester containing *p*-NN-OEt complexes. Similar trends were observed for other concentrations of water (Figure S4).

served for the *meta*-substituted complexes (Figure 5); measurably slower rates are observed for the amino acid and amino acid ester substituted complexes. A similar trend is found for the *para*-substituted complexes, where the amino acid and amino acid ester complexes have slower rates than the other *para*-substituted catalysts, but the step function is not observed, possibly due to other effects such as slower electron transfer, described in more detail below. This observation suggests a clear role for the amide functionality in hydrogen production. While the amide bond appears to have an influence on rates, the ligand size, polarity and aromaticity do not contribute significantly to the rates of hydrogen production, and suggest that design principles that attempt to modify the dielectric constant near the metal will not result in substantial rate enhancements due to this effect alone.

A possible role of the amide functional group could be to concentrate water and/or protons around the catalyst. This could also be the role of dipeptide complexes containing acidic and basic functional groups reported previously.[10b] To further investigate this possibility, MD simulations were performed on three representative complexes in acetonitrile at various water concentrations. Complexes with no amide, *m*/*p*-NN-OEt, and with an amide, *m*/*p*-NNA-AlaOEt, were studied. Additionally, a dipeptide complex containing the basic amino acid lysine, *m*/*p*-NNA-Lys, the fastest dipeptide catalyst reported to date,[10b] was also studied, in its protonated form.

Water was observed to interact extensively with the protonated amino group of lysine, and, consequently, concentrate more strongly near the surface of the *m*/*p*-NNA-Lys catalyst (green lines in Figure 6). This finding provides evidence that, in acetonitrile solutions, charged amino groups are able to concentrate water, consistent with our hypothesis. In contrast, the water distribution around the *m*/*p*-NN-OEt and *m*/*p*-NNA-AlaOEt complexes is not significantly different from the bulk, aside from small fluctuations close to the complex surface (blue and red lines in Figure 6), with any differences being within our statistical uncertainty. Movies from the MD simulations showing the distribution of water around *p*-NNA-Lys and *p*-NNA-AlaOEt are provided in the Supporting Information.

The effect of water on catalytic rates: The addition of water resulted in more significant rate enhancements for the functionalized amino acid and dipeptide substituted complexes reported here (as much as 7.5 times) than observed for the parent complex (1.3 times), and are reminiscent of the previously reported complex having a -$CH_2P(O)(OEt)_2$ substituent at the *N*-phenyl *para*-position (rates were reported as 1850 vs 500 s^{-1} under dry conditions).[7b] The rates for all of these complexes in the absence of water are slower than for the parent catalyst, suggesting a limitation in these catalysts, possibly steric, that is not present in the parent catalyst and that is overcome by the presence of water.

The role of substituent size and positioning: Electrochemistry studies: As shown in Figure 4, catalytic currents, and thus TOF's, increase more rapidly with increasingly negative applied potential for the *meta*-substituted (Figure 4B) versus the *para*-substituted (Figure 4A) complexes. This correlation, observed for all of the systems examined under both wet and dry conditions, is illustrated in Figure 7 and Table 1

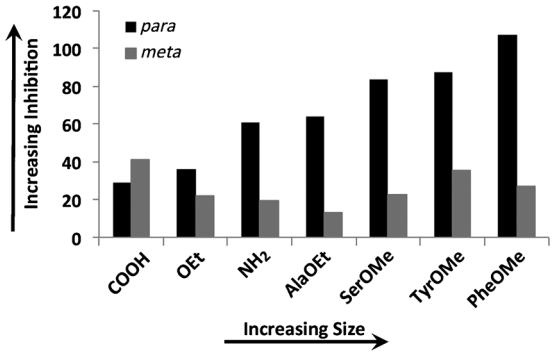

Figure 7. Comparing the % increase in TOF as a function of overpotential (Table 1 and equation therein), the *para*-substituted complexes (black) show that larger complexes are more inhibited at lower overpotentials, indicating that more energy is required to turn larger catalysts over. The same trend is not observed for the *meta*-substituted complexes (blue).

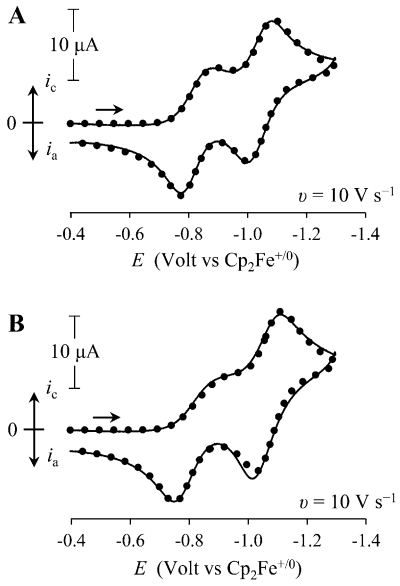

Figure 8. Cyclic voltammograms of A) *meta*- and B) *para*-NNA-TyrOMe complexes (0.7 mM) in acetonitrile (0.2 M nBu$_4$N$^+$BF$_4^-$) without added acid. Experimental data (background-subtracted, black lines) was collected at a 1 mm dia. glassy carbon electrode; simulated voltammograms (red circles) were obtained by least-squares refinement of electron transfer kinetic parameters.

by a comparison of TOF values at −0.9 and −1.1 V versus $Cp_2Fe^{+/0}$. This is not due to resistance effects since the maximum catalytic currents for the *meta*- and *para*-complexes are the same. The *meta*-substituted complexes show little inhibition at moderate potentials, and the degree of inhibition shows essentially no substituent size dependence. In contrast, the *para*-substituted complexes show a marked inhibition that is more severe with larger substituents, suggesting that the effect is unique to the *para*-substituted systems and is steric in origin.

The observation of plateau currents in voltammograms of electrocatalytic systems, such as that seen in Figure 4B, is consistent with steady-state reaction kinetics with rapid electron transfer. Electron transfer rates generally increase exponentially with increasing applied potential.[13] At sufficiently high potentials, electron transfer is rapid compared to turnover and the current becomes a function of the rate of chemical steps in the catalytic cycle.[14] For electron transfers with larger barriers, a larger overpotential is required; for an electrocatalytic system, this will register as a more gradual increase in current with applied potential, such as that seen in Figure 4A, consistent with the observations reported here.

To test the hypothesis that slow electron transfer is responsible for the observed substituent positioning effect on the increase of current with applied potential (Figure 4, Table 1), we examined the voltammetry of *m*/*p*-NNA-TyrOMe and *m*/*p*-NNA-SerOMe catalysts without added substrate as a function of the scan rate (scan rate v = 1–40 V s^{-1}). Figure 8 shows voltammograms obtained at 10 V s^{-1} along with digital simulations for *m*/*p*-NNA-TyrOMe. Experimental and simulated voltammograms of the *m*/*p*-NNA-TyrOMe complexes at the lowest and highest scan rates are shown in Figure S5.

These voltammograms show a substantial difference in the shape of the $Ni^{II} \rightarrow Ni^{I}$ reduction wave, with the peak of this wave merging into the $Ni^{I} \rightarrow Ni^{0}$ wave for the *para*-substituted complex. This is consistent with a difference in electron transfer rates, as borne out in digital simulations of these voltammograms. The estimated values of k_s (the electron transfer rate constant at $E = E°$ for the $Ni^{II/I}$ couple) were 0.036(4) and 0.0132(2) cm s^{-1}, respectively, for the *meta*- and *para*-substituted complexes (confidence intervals at the 2 × σ level), with Butler–Volmer transfer coefficients α of 0.214(9) and 0.270(5) (Table S3). Electron transfer was found to be considerably faster for the $Ni^{I/0}$ redox couples of both the *meta*- and *para*-substituted complexes; kinetic parameters were statistically indistinguishable, with k_s = 0.126(9) and 0.136(9) cm s^{-1} and α = 0.34(3) and 0.30(3), respectively. The digital simulation and least-squares refinement procedures are described in the Experimental Section.

To examine the influence of electron transfer kinetics on the catalytic response, we used the above estimates of k_s and α to model a prototypical EC′ catalytic reaction. The model consisted of a reduction of the catalyst by one electron at the electrode and a chemical re-oxidation of the catalyst by a substrate molecule occurring at a rate of 250 s^{-1}, approximately as observed for these catalysts without added water. Complete simulation parameters are given in Table S5. The resulting simulated catalytic waves, along with the response expected for fast electron transfer, are shown in Figure 9A. The experimentally observed responses (cathodic sweep only) are shown in Figure 9B. The qualitative similarity between the simulated and experimental catalytic waves shown in Figure 9 indicates that the difference in electron transfer kinetics determined for these catalysts will result in differences in the catalytic responses that are similar in kind and in magnitude to those observed experimentally.

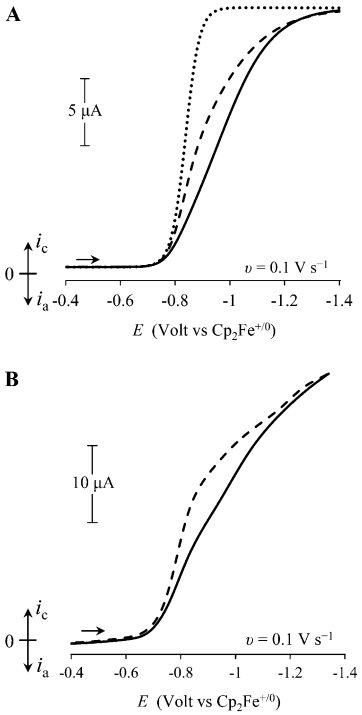

Figure 9. A) Simulated cyclic voltammograms for a prototypical one-electron electrocatalytic process (TOF = 250 s^{-1}) with electron transfer kinetic parameters k_s and α as estimated by digital simulation for the $Ni^{II/I}$ redox couple of *meta*-NNA-TyrOMe (dashed trace), *para*-NNA-TyrOMe (solid trace), and for a fast electron transfer ($k_s = 1 \times 10^4$ cm s^{-1}, $\alpha = 0.5$; dotted trace; see Table S5 for details). B) Corresponding experimental cyclic voltammograms (cathodic sweep only) for *meta*- (dashed trace) and *para*-NNA-TyrOMe (solid trace) in MeCN (0.1 M $nBu_4N^+PF_6^-$) with sufficient acid to afford pseudo-first order kinetics, and with no added water. The simulated voltammograms shown in panel A were *not* obtained by refinement against the data in panel B. These data provide strong evidence that electron transfer kinetics explain the observed differences in the catalytic waves for *meta*- and *para*-substituted complexes.

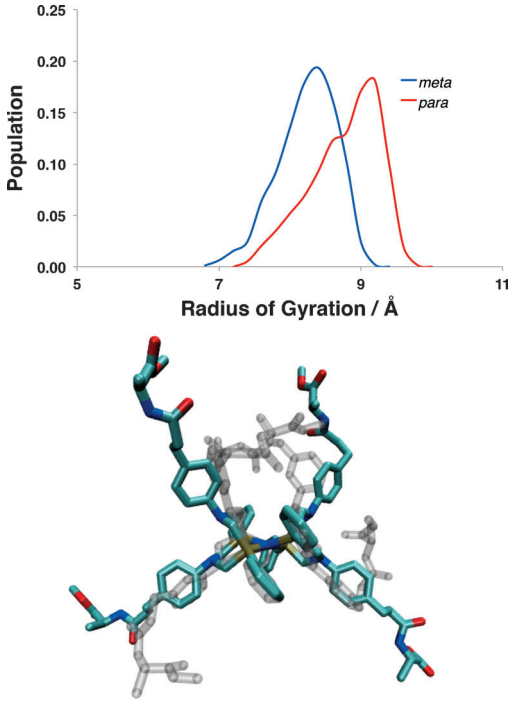

Figure 10. Probability distribution of the radius of gyration for the *m*/*p*-NNA-AlaOEt complexes shows that the *meta*-substituted complex is more compact than the *para*-substituted complex. Representative structures from the molecular dynamics trajectories are shown below (the *m*-NNA-AlaOEt structure is gray and transparent).

A similar analysis was performed with the *m*/*p*-SerOMe complexes. A smaller but statistically significant difference in the $Ni^{II/I}$ electron transfer kinetic parameters for the *meta* and *para*-substituted complexes was observed for these complexes as well. Estimates of k_s were 0.085(4) and 0.043(3) cm s^{-1} for the *meta*- and *para*-substituted complexes, respectively, with α values of 0.18(2) and 0.24(1) (Table S4). For the $Ni^{I/0}$ couples, initial refinements afforded $k_s > 0.2$ cm s^{-1}, and large confidence intervals for both k_s and α. This suggested that electron transfer for the $Ni^{I/0}$ was under equilibrium control for both complexes at all scan rates. Experimental and simulated voltammograms of the *m*/*p*-NNA-SerOMe complexes at the lowest and highest scan rates are shown in Figure S6.

The role of substituent positioning: Computational modeling: To provide insight into the role of substituent positioning (*meta* vs. *para*) on the rate of electron transfer, geometrical parameters from MD simulations on the *m*/*p*-NNA-AlaOEt complexes were analyzed. Our simulations showed minimal differences in the geometry of the $[Ni(P^{Ph}_2N^{Ph}_2)_2]^{2+}$ core. However, the radius of gyration,[15] which provides a measure of the compactness of the molecules, was found to be different for the two complexes, where the *meta*-substituted complex was observed to be more compact (Figure 10).

The compactness of the *meta*-substituted complexes is due to the substituents folding around the outside of the catalyst instead of pointing outward from the catalyst as observed in the *para*-substituted complexes. In addition, the *meta*-substituted complex displays a larger flexibility of the dipeptide chains as indicated by the root mean square displacement from the average structure of 3.47 Å when compared to the corresponding quantity for the *para*-substituted complex of 2.50 Å. The different flexibility of the two complexes is shown with an overlay of the MD trajectories in Figure 11. Ni^{I} complexes show similar properties (data not shown).

Amino acids as proton relays: To explore whether the dipeptide substituents can act as proton relays, we carried out umbrella sampling free energy simulations for the *m*/*p*-NNA-Lys and *m*/*p*-NNA-AlaOEt (Figure 12). In the *para*-substituted complexes, the energetic cost to bring the carboxylic acid functionality of *p*-NNA-Lys or the carbonyl oxygen of the ester group of *p*-NNA-AlaOEt (N-to-O contact) within hydrogen bonding distance (~3.5 Å) of the pendant amine is 7.5 and 5.6 kcal mol^{-1}, respectively. Both of the *meta*-substituted complexes, *m*-NNA-Lys and *m*-NNA-AlaOEt complexes show even smaller energy costs

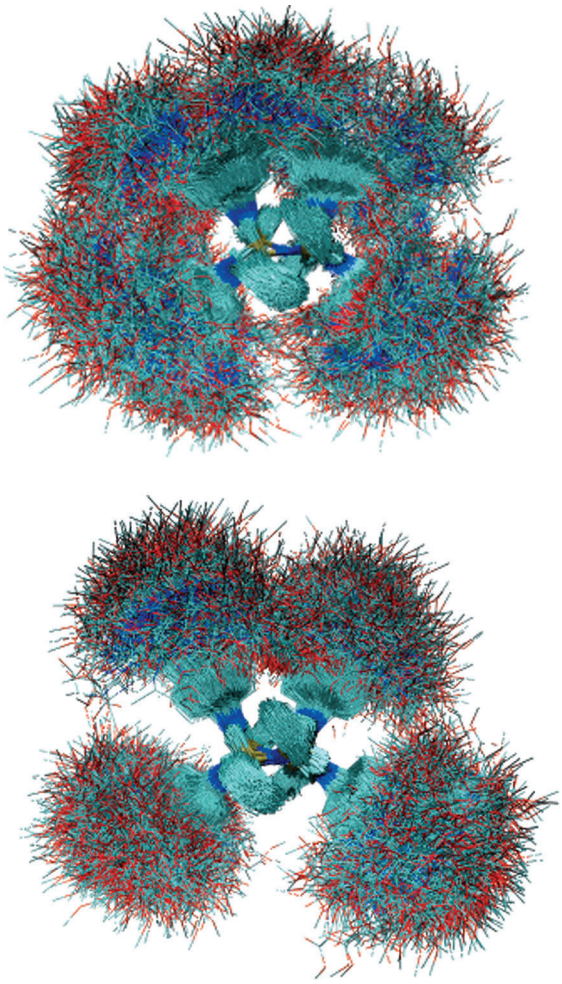

Figure 11. Overlay of the structures from MD trajectories of the *meta*- (top) and *para*- (bottom) substituted NNA-AlaOEt catalysts. The unconstrained nature of the dipeptide ligands is evident based on the large phase space covered. The *meta*-substituted complex is more flexible then the *para*-substituted complex, evidenced by the *meta*-substituted ligands accessing the full space around the $Ni(P^{Ph}h_2N^{Ph}{}_2)_2{}^{2+}$ core.

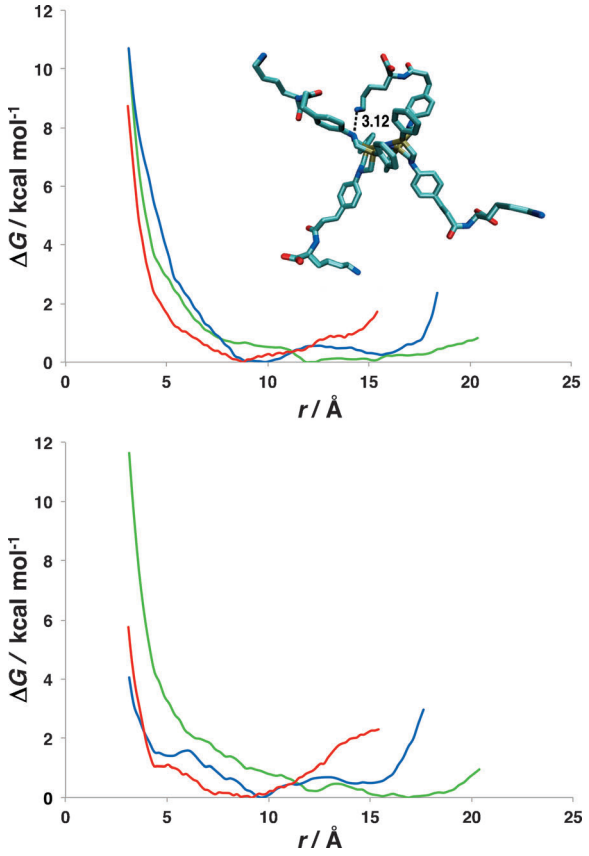

Figure 12. Relative free energy cost to bring the functional groups of the peptide substituents within hydrogen bonding distance (3.5 Å) of the pendant amine for (top) *para*-substituted complexes and (bottom) *meta*-substituted complexes. The energy of the complex as a function of the N-to-O distance, where N is the pendant amine and O is the carbonyl oxygen on the alanine ester or on the carbonyl oxygen of the acid on lysine, are shown in red and blue, respectively. The green line shows the free energy as a function of the N-to-N distance for the *m*/*p*-NNA-Lys complexes (between the pendant amine and the protonated amino group, shown in the insert for *p*-NNA-Lys). These data show that the outer-coordination sphere amino acids can act as proton relays to deliver protons to the pendant amine.

for the N-to-O contact than the corresponding *para*-substituted counterparts, with values of 2.8 and 3.6 kcal mol^{-1}, respectively. The reduced energy cost might be a consequence of the more compact nature of the *meta*-substituted ligands. While the barriers for both *meta*- and *para*-substituted complexes are low enough to be accessed by structural fluctuations of the molecule, in no case were *stable* interactions (minima on the free energy surface) observed between the functional groups of the substituents and the pendant amine.

The energy cost to bring the protonated amino group of the lysine for the *m*/*p*-NNA-Lys complex within ~3.5 Å of the pendant amine was also investigated. This was found to be 8.5 kcal mol^{-1} for both the *meta*- and *para*-substituted complex (Figure 12, N-to-N contact), also reasonably accessible via thermal fluctuations of the molecule in solution. The similarity in this case between the *meta*- and *para*-substituted complexes is due to the protonated amino group of the lysine in both complexes preferring to interact with the surrounding medium (acetonitrile and water). The larger energies observed for the N-to-N contact as compared to the N-to-O contacts are most likely due to the insufficient energy gain from forming a hydrogen bond with the pendant amine, that does not compensate for the loss of the conformational entropy and the reduced interaction with the environment.

The significant difference in the energy cost between the *meta*- and *para*-substituted complexes to achieve an N-to-O contact indicates that the *meta*-substituted complexes have easier access to the pendant amines. If protonation of the pendant amines involves a proton transfer from protonated carboxyl or carbonyl groups, a faster catalytic rate would be expected for the *meta*-substituted complexes. Since this is not observed experimentally (Table 1), we propose that the protons are not likely delivered to the pendant amine in this manner. Proton transfer from the protonated amino group of *m*/*p*-NNA-Lys complexes is accessible since the free

energy cost of 8.5 kcal mol^{-1} to achieve the N-to-N contact can be thermally overcome, and is a possible proton transfer pathway.

Discussion

Metalloenzymes are highly efficient catalysts, performing a wide variety of chemically challenging reactions with an overall efficiency typically exceeding that of their molecular catalyst counterparts. The active site of the enzyme (the primary-coordination sphere) unquestionably plays an essential role in catalysis. However, the secondary-coordination sphere, including atoms close to but not directly interacting with the metal, and the outer-coordination sphere which includes the rest of the protein scaffold, also play essential roles in the resulting catalytic process. In enzymes, the outer-coordination sphere participates in catalysis by controlling selective substrate transport and electron transfer as well as by controlling reactivity with subtle influences such as hydrogen bonding stabilizing unusual ligand structures, controlling the redox potential of the metal or the pK_a of a given residue.[1,16] NMR and X-ray crystallography have elucidated many of the complex features of the protein scaffold in enzymes, but there is still much to be learned about how enzymes function with such apparent simplicity, with potential applications to improving molecular catalysts. Because they contain fewer functionalities, molecular catalysts provide a reasonable scaffold with which to test some of these features.

Understanding the role that chemically attached functional groups in the outer-coordination sphere can have on controlling the environment around the active site of molecular catalysts and developing mechanistic insight into the observed phenomenon are important goals. The studies reported herein were undertaken to evaluate the role of individual amino acid functional groups, to increase the diversity of amino acid functional groups studied so further trends could be established, and to assess whether re-positioning the dipeptide would influence catalysis. Combining the studies here with the observations from previous work allows us to develop a mechanism for the contribution of the unconstrained outer-coordination sphere introduced into these molecular catalysts.

The role of functional groups on hydrogen production: The presence of polar or aromatic side chains has no measurable impact on rate when compared to their non-polar or non-aromatic counterparts (serine and alanine, or tyrosine and phenylalanine, for example; Table 1). This is in contrast to previous findings that show the importance of similarly positioned acidic or basic groups in enhancing catalytic rates (Table S6, taken from Jain et al.).[10b] This suggests that the global dielectric or π-interactions created by the nearby, but unconstrained polar or aromatic groups, do not have a significant influence on the catalytic activity. Metalloenzymes have been shown to be influenced by outer-coordination sphere π-interactions from phenylalanine and tyrosine residues,[2e] and polar groups are shown to be important in stabilizing active sites.[2f] The dielectric effect of the outer-coordination sphere has also been proposed to be important in enzymes.[1,2d] The results obtained here suggest that the global dielectric around the active site is not important for influencing catalysis in the present systems.

Non-natural amino acid esters in either the *meta*- or *para*-position resulted in rates only slightly faster than the parent catalyst. The presence of an amide bond results in a nearly uniform increase in rate of 40% (Figure 5 and Table 1). Because we investigated the C-terminal esterified version of the dipeptide, eliminating an influence from a free acid group, and because we see no influence on catalysis with the addition of polar or aromatic groups, the increase in rate can be attributed to the presence of the amide functional group.

Consideration of the present data alongside prior results reveals interesting trends. The order of rate enhancement versus functional group is summarized as follows: bases > acids > amides > esters. Amide functional groups enhance catalysis while ester groups appear to have a negligible effect. For instance, previously reported data (Table S6)[10b] show that the protected aspartic acid and glutamic acid substituted complexes have similar rates to the protected alanine and phenylalanine complexes reported in this paper. They both have two esters instead of one, neither of which shows an enhancement in rate. Multiple amides, found in the lysine(Boc)OMe substituted complex (Table S6), enhance rates even more than a single amide. In contrast to esters, free acids do enhance catalysis, increasing the observed rates by 1.5 to 3 times. Free amines increase the rates even more than free acids, as the lysine substituted complex demonstrates.

Our mechanistic interpretation is that the amino acid/ester complexes help to concentrate protons and water, and in some cases enhance proton delivery. This is demonstrated with our computational models, which show that the lysine substituted complex, the fastest amino acid substituted catalyst to date, shows a significant increase in water concentration compared to the *p*-NN-OEt or the *p*-NNA-AlaOEt. The increased local concentration of protons and water could enhance catalysis alone, since both water and protons are shown to increase catalytic rates.[7b,10a] Additionally, MD studies of the *p*-NNA-Lys complex suggest that thermal fluctuations in the dipeptide substituents may bring them close enough to deliver a proton directly to the pendant amine. The unconstrained nature of the ligands necessitates that this would be a transient conformation, however, the low energy cost to achieve this structural rearrangement suggests that proton delivery may be occurring through this pathway some of the time, at least for the basic and possibly acidic complexes, if not for the ester terminated complexes. The faster rates observed for complexes with basic amino acids compared to those with acidic amino acids may be partially due to the lower pK_a of amines in acetonitrile (~17–20 vs ~20–25)[17] lowering the barrier for proton delivery.

A similar ability to concentrate water was not computationally predicted for the *p*-NNA-AlaOEt, a complex containing an amide bond that is shown to enhance catalysis. We speculate that the amide bond is enhancing catalysis by a similar mechanism, but that the computational studies are insensitive to the smaller changes in rate for complexes containing an amide (~40%) compared to the lysine substituted complex (350%), due to the statistical error inherent to those studies. It is also possible that the neutral amide is more able to concentrate protons than water, an investigation outside the scope of this study.

Effect of substituent positioning on H_2 production: Dipeptide substituents were attached in both *meta*- and *para*-positions of the catalyst *N*-phenyl groups to examine the role of the outer-coordination sphere structure and connectivity on catalytic rates and overpotentials. As seen in Table 1, substituent positioning did not influence the rates of hydrogen production at large applied potentials but showed a substantial effect on the potentials needed to achieve these rates. All of the *para*-substituted complexes required larger applied potentials to attain maximal turnover frequencies, as noted previously.[10b]

This observation is hypothesized to reflect a difference in electron transfer kinetics. If electron transfer is fast compared to turnover, the current will rise rapidly over a narrow range of potentials, as illustrated in the simulated catalytic wave shown in Figure 9A, dotted trace. Slow electron transfer can be overcome by the application of larger potentials, so the rate of increase in current with applied potential reports on the rate of electron transfer compared to turnover. Digital simulation of CVs collected with *m*/*p*-NNA-SerOMe and *m*/*p*-NNA-TyrOMe complexes with scan rates from 1 to 40 $V s^{-1}$ in the absence of acid revealed faster electron transfer rates for the *meta*-substituted serine and tyrosine complexes than the *para*-substituted complexes (Figure 8, S5 and S6). Simulated cyclic voltammograms of a prototypical one electron catalytic process using these electron transfer rate estimates showed that overpotentials at $E_{p/2}$ increase with slower electron transfer, in agreement with the experimental observations (Figure 9).

Redox kinetics could be influenced either by ligand size, with larger ligands limiting the proximity of the metal center to the electrode, or through steric or hydrogen bonding interactions between ligands that could influence rearrangement barriers. The reduction of Ni^{II} to Ni^{I} in particular forces a change in the phosphine binding geometry from roughly square planar to tetrahedral,[18] so electron transfer kinetics would be more evident for the $Ni^{II/I}$ couple than for the $Ni^{I/0}$ couple. The $Ni^{I/0}$ couples for the serine substituted complexes were too fast to measure with the present data, however with the tyrosine-substituted systems, the $Ni^{II/I}$ couple shows a positioning effect whereas the $Ni^{I/0}$ couple does not, supporting the rearrangement hypothesis. If proximity to the electrode were the dominant effect, the larger complexes would be expected to have slower electron transfer for both the $Ni^{II/I}$ and the $Ni^{I/0}$, as is also observed in comparing the larger tyrosine complexes with the smaller serine complexes. Computational modeling suggests that there is a comparative compactness of the *meta*-substituted complexes, however, this structural difference could also influence both rearrangement and proximity. Therefore, the present results indicate that ligand size effects on proximity of the Ni center to the electrode and intramolecular interactions influencing barriers to rearrangement cannot be distinguished and may both contribute to the observed electron transfer rate. Nonetheless, the electrochemistry experiments provide compelling evidence that the higher overpotential needed for the *para*-substituted complexes is due to slower electron transfer than for the *meta*-substituted complexes. Of significance is that the overpotential can be recovered by modifying the positioning; this is a significant advancement in our understanding of the outer-coordination sphere on molecular catalysts.

Providing insight into the enzyme: The lack of dependence of the rates on the polarity of the dipeptide is somewhat unexpected given the ability of these groups to form hydrogen bonds which would allow them to concentrate water or protons. It is also unexpected in light of the highly hydrophobic nature of the [NiFe]-hydrogenase active site, 30% of which is due to polar side chains such as serine and tyrosine. It does suggest that a *global* dielectric effect is not important to catalysis in the molecular catalysts mimic, and may also not play an important role in the enzyme. However, the *local* dielectric created by the precise positioning afforded by the large protein scaffold in hydrogenase is likely an essential aspect of the outer-coordination sphere that is not achieved in the molecular catalysts reported here, demonstrated by the conformational freedom of the dipeptides shown in Figure 11. The impact of positioning in the *meta*- versus *para*- orientation highlights the influence of positioning within the chemical bonding framework. Positioning within the 3-dimensional framework is expected to be equally important, as demonstrated by the transient proton delivery from the flexible dipeptide to the pendant amine. Future efforts to constrain the position of specific side chains will be important in evaluating this effect in hydrogenase enzymes, as well as in molecular catalyst mimics. Overall, the insights gained here suggest that the structured protein scaffold provides advantages in both atomic control of the environment around the active site as well as maintaining facile electron transfer.

Conclusion

Twelve new catalysts for hydrogen production containing a peptide based outer-coordination sphere have been synthesized and characterized electrochemically, structurally and computationally. The outer-coordination sphere has been shown to modulate both rates and overpotentials of hydrogen production. The bulky dipeptide ligands increased barriers to electron transfer and thus required higher overpoten-

tials for catalysis compared to the unmodified complex, with the largest effect seen for the *para*-substituted complexes. Re-positioning the dipeptide resulted in recovering the lower operating potential, due to the more compact structure of the *meta*-substituted species. Polar or aromatic side chains, in the absence of acidic backbone groups, did not appear to enhance catalysis beyond the addition of the amide group, implying that a global dielectric does not enhance catalysis. However, amide, acidic or basic groups do enhance catalysis up to five-fold, which we attribute to the ability of these functional groups to concentrate water and protons near the active site and to facilitate proton transfer. While the global effects observed here are important, the results suggest that the precise positioning afforded by the protein scaffold is important in affording fast rates at low overpotentials.

Experimental Methods

Instrumentation and methods: ^{1}H and $^{31}P\{^{1}H\}$ NMR spectra were recorded on Varian VNMRS or Inova spectrometers operating at 300 MHz or 500 MHz ^{1}H frequency at 23 °C. All ^{1}H signals were internally referenced to the residual solvent protons and ^{1}H TOCSY were used to assign the ^{1}H spectra. The $^{31}P\{^{1}H\}$ NMR spectra were externally referenced to phosphoric acid (0 ppm). Electrospray ionization (ESI) and chemical ionization (CI) mass spectra were collected at the Indiana University Mass Spectrometry Facility on a Waters/Micromass LCT Classic using anhydrous solvents and inert atmosphere techniques. MALDI-MS were collected on a Waters LR used in reflectron mode, with α-cyano-4-hydroxycinnamic acid as the matrix, at the Protein Chemistry Technology Center, University of Texas, Dallas, TX. Elemental analyses were carried out by Atlantic Microlab, Norcross, Ga.

Materials: All reactions were performed under an inert atmosphere of nitrogen using standard Schlenk techniques or in a glove box. Solvents were de-oxygenated and purified using an Innovative Technology, Inc. PureSolv solvent purification system. [D_3]-Acetonitrile (Cambridge Isotope Laboratories, 99.5% D) was vacuum-distilled from P_2O_5. $CDCl_3$ (Cambridge Isotope Laboratories, 99.5% D) was degassed and stored over molecular sieves. Water was dispensed from a Millipore MilliQ purifier at 18 MΩ and sparged with nitrogen. 2-(1*H*-Benzotriazole-1-yl)-1,1,3,3-tetramethyluronium tetrafluoroborate (TBTU), 3-(4-aminophenyl)propionic acid, 3-(3-aminophenyl)propionic acid, ammonium chloride and trimethylsilyl chloride (Aldrich) were used as received. Diisopropylethyl amine (DIPEA) (Aldrich) was degassed prior to use by the freeze-pump-thaw method. The amino acid esters were purchased from Nova Biochem or Sigma Aldrich and used as received. Tetraethylammonium tetrafluoroborate (Alfa-Aesar) was recrystallized twice from hot ethanol; the crystals obtained were dried under vacuum. Ferrocene (Aldrich) was sublimed under vacuum before use. Dimethylformamide-trifluoromethanesulfonic acid, $DMFH^{+}$, was prepared by the method of Favier and Duñach.[19] $[Ni(MeCN)_6](BF_4)_2$ and $P^{Ph}{}_2N^{m/p\text{-}NNA}{}_2$ (where *p*-NNA = 3-(4-aminophenyl)propionic acid and *m*-NNA = 3-(3-aminophenyl)propionic acid) were prepared following literature methods.[20]

Syntheses

Ligands: *3-(3-Aminophenyl)propionic acid ethyl ester*: This compound was synthesized following a previously published procedure. Excess trimethylsilyl chloride (15.6 mmol) was added dropwise to a stirred solution of 3-(3-aminophenyl)propionic acid (0.50 g, 3.27 mmol) in ethanol (10 mL) at 0 °C. This mixture was then allowed to warm to room temperature and let stir for an additional three hours. Then diethyl ether (10 mL) was added and washed with a saturated sodium bicarbonate solution. The organic layer was collected and dried over anhydrous magnesium sulfate. The solution was filtered and the solvent was removed under vacuum to yield a dark yellow oil (216 mg, 1.19 mmol, 36%). ^{1}H NMR (CD_2Cl_2): δ = 7.11, 6.61, 6.54 (m, 4H, N-Ph), 4.14 (q, 2H, $COOCH_2$), 3.73 (b, 2H, NH_2), 2.87 (dd, 2H, N-PhCH_2), 2.61 (dd, 2H, CH_2COO), 1.27 ppm (t, 3H, CH_2CH_3).

$P^{Ph}{}_2N^{mNNA}{}_2$: To ethanol (100 mL) was added bismethylhydroxy phenylphosphine (0.515 g, 3.03 mmol) and 3-(3-aminophenyl)propionic acid (0.500 g, 3.03 mmol). The solution was slowly heated to 76 °C and allowed to stir overnight. The resulting white precipitate was collected and washed with ethanol and diethyl ether and dried in vacuo (0.81 g, 1.35 mmol, 89%). The compound was not soluble in common organic solvents but was soluble in basic chloroform (pH > 10). $^{31}P\{^{1}H\}$ NMR (basic $CDCl_3$): δ = −54.66 ppm (s); ^{1}H NMR (basic $CDCl_3$): δ = 7.66–6.50 (m, 18H, P-Ph, N-Ph), 4.45 (dd, 4H, PCH_2N), 3.95 (dd, 4H, PCH_2N), 2.86 (m, 4H, CH_2C(O)N), 2.62 ppm (m, 4H, N-PhCH_2); $P^{Ph}{}_2N^{mNN\text{-}OEt}{}_2$ was prepared in an analogous manner, see Supporting Information.

$P^{Ph}{}_2N^{pNN\text{-}NH2}{}_2$: 3 equiv TBTU (241 mg, 0.752 mmol) and 3 equiv HOBT (102 mg, 0.752 mmol) were added to a dichloromethane solution containing one equivalent of $P^{Ph}{}_2N^{pNNA}{}_2$ (150 mg, 0.251 mmol) and 8 equiv DIPEA (258 mg, 2.0 mmol). The mixture was stirred for 20 min and then 4 equiv ammonium chloride (54.0 mg, 1.0 mmol) were added and stirred overnight. The resulting white solid was filtered off and washed with copious amounts of water to remove any residual ammonium chloride, followed by washing with acetonitrile and diethyl ether. The resulting white solid was collected and dried in vacuo (121.9 mg, 0.205 mmol, 82%). $^{31}P\{^{1}H\}$ NMR ([D_6]DMSO): δ = −51.10 ppm (s); ^{1}H NMR ([D_6]DMSO): δ = 7.68–7.5 (m, 10H, P-*Ph*), 7.22 (s, 2H, C(O)NH_2), 7.00 (dd 4H, N-Ph(*m*)), 6.69 (s, 2H, C(O)NH_2), 6.59 (d, 4H, N-Ph(*o*)), 4.53 (m, 4H, PCH_2N), 4.12 (m, 4H, PCH_2N), 2.64 (m, 4H, CH_2C(O)N), 2.24 (m, 4H, N-PhCH_2); elemental analysis (%) calcd for: C 68.44, H 6.42, N 9.39; found: C 68.14, H 6.23, N 9.48; $P^{Ph}{}_2N^{mNN\text{-}NH2}{}_2$ was prepared in an analogous manner; see Supporting Information.

$P^{Ph}{}_2N^{pNNA\text{-}AlaOEt}{}_2$ *(AlaOEt*=DL-*alanine ethyl ester):* 2 equiv TBTU (161 mg, 0.502 mmol) and 2 equiv HOBT (60 mg, 0.502 mmol) were added to a dichloromethane solution containing one equivalent of $P^{Ph}{}_2N^{pNNA}{}_2$ (150 mg, 0.251 mmol) and 2.2 equiv DIPEA (71.1 mg, 0.552 mmol). The mixture was stirred for 20 min and then 2 equiv DL-alanine ethyl ester hydrochloride (77.0 mg, 0.502 mmol) were added and stirred overnight. The solution was extracted with water to remove residual chloride and dried over anhydrous magnesium sulfate. The solution was passed through celite and the solvent was removed under vacuum. The resulting yellow/white solid was washed with acetonitrile and recrystallized from diethyl ether/dichloromethane (4:1). The resulting white solid was collected and dried in vacuo (80.3 mg, 0.10 mmol, 40%). $^{31}P\{^{1}H\}$ NMR ($CDCl_3$): δ = −50.05 ppm (s); ^{1}H NMR ($CDCl_3$): δ = 7.60 (m, 2H, P-Ph(*p*)), 7.50, 7.48 (m, 8H, P-Ph(*o,m*)), 7.03 (dd 4H, N-Ph(*m*)), 6.64 (d, 4H, N-Ph(*o*)), 5.99 (d, 2H, C(O)N*H*), 4.53 (m, 2H, α*CH*), 4.44 (m, 4H, PCH_2N), 4.17 (q, 4, $COOCH_2CH_3$), 4.00 (dd, 4H, PCH_2N), 2.83 (m, 4H, CH_2C(O)N), 2.43 (m, 4H, N-PhCH_2), 1.31 (d, 6H, βCH_3), 1.23 ppm (t, 6H, CH_2CH_3); elemental analysis (%) calcd for: C 6.32, H 6.83, N, 7.03; found: C 66.26, H 6.95, N 7.07.

All of the following dipeptide ligands were prepared in an analogous manner to the $P^{Ph}{}_2N^{pNNA\text{-}AlaOEt}{}_2$ preparation described above, with complete details in the Supporting Information: $P^{Ph}{}_2N^{m/pNNA\text{-}SerOMe}{}_2$ (SerOMe = L-serine methyl ester), $P^{Ph}{}_2N^{m/pNNA\text{-}PheOMe}{}_2$ (PheOMe = L-phenylalanine methyl ester), $P^{Ph}{}_2N^{m/pNNA\text{-}TyrOMe}{}_2$ (TyrOMe = L-tyrosine methyl ester), $P^{Ph}{}_2N^{mNNA\text{-}AlaOEt}{}_2$ (AlaOEt = DL-alanine ethyl ester).

Metal complexes:*[Ni($P^{Ph}{}_2N^{pNN\text{-}NH2}{}_2$)$_2$](BF$_4$)$_2$*: The purified $P^{Ph}{}_2N^{pNN\text{-}NH2}{}_2$ ligand (68.4 mg, 0.115 mmol) was added to an acetonitrile solution containing 0.5 equiv $[Ni(MeCN)_6](BF_4)_2$ (27 mg, 0.057 mmol) and stirred for 24 h. The resulting red solution was filtered through celite and the solvent was removed under vacuum. The residual red oil was then re-dissolved in a minimal amount of acetonitrile (~2 mL) and added dropwise to 0 °C diethyl ether (~30 mL) and stirred in an ice bath until all of red solid had precipitated out of the acetonitrile/diethyl ether solution. The resulting red solid was filtered, washed with diethyl ether and dried in vacuo (78 mg, 0.055 mmol, 95%). $^{31}P\{^{1}H\}$ NMR (CD_3CN): δ = 5.32 ppm (s); ^{1}H NMR (CD_3CN): δ = 7.44–7.19 (m, 36H, P-Ph, N-Ph), 6.18 (s, 4H, C(O)NH_2), 5.67 (s, 4H, C(O)NH_2), 4.24 (m, 8H, PCH_2N), 3.93 (m, 8H,

PCH_2N), 2.91 (dd, 8H, $CH_2C(O)N$), 2.50 ppm (dd, 8H, N-PhCH_2); MALDI MS: m/z: calcd for $\{[Ni(P^{Ph}{}_2N^{pNN\text{-}NH2}{}_2)_2]\}^{2+}$: 1251.58; found: 1250.41 $[M^{2+}-H^+]$.

All of the metal complexes were prepared in an analogous manner to the $[Ni(P^{Ph}{}_2N^{pNN\text{-}NH2}{}_2)_2](BF_4)_2$ preparation listed above, with complete details in the Supporting Information: $[Ni(P^{Ph}{}_2N^{m/pNNA\text{-}AlaOEt}{}_2)_2](BF_4)_2$, $[Ni(P^{Ph}{}_2N^{m/pNNA\text{-}SerOMe}{}_2)_2](BF_4)_2$, $[Ni(P^{Ph}{}_2N^{m/pNNA\text{-}PheOMe}{}_2)_2](BF_4)_2$; $[Ni(P^{Ph}{}_2N^{m/pNNA\text{-}TyrOMe}{}_2)_2](BF_4)_2$, $[Ni(P^{Ph}{}_2N^{m/pNNA}{}_2)_2](BF_4)_2$, $[Ni(P^{Ph}{}_2N^{m/pNN\text{-}OEt}{}_2)_2](BF_4)_2$; $[Ni(P^{Ph}{}_2N^{m/pNN\text{-}NH2}{}_2)_2](BF_4)_2$.

Electrochemistry: All electrochemical studies were done in a N_2 glove box in 0.2 M $Et_4N^+BF_4^-$ acetonitrile solution at the ambient temperature of the glovebox, 24–27 °C, using ferrocene as an internal standard unless otherwise stated. Cyclic voltammetry experiments were performed on a CH Instruments 1100A or 600D electrochemical analyzer using a standard three-electrode configuration. The working electrode was a 1 mm diameter glassy carbon disk coated in PEEK (Cypress Systems EE040), polished between scans using 0.25 μM MetaDi II diamond polishing paste (Buehler) on a Buehler MicroCloth lubricated with 18 MΩ water, and the counter electrode was a 3 mm glassy carbon rod (Alfa-Aesar). The reference electrode was a platinum wire (Alfa-Aesar). All couples were referenced to the ferrocenium/ferrocene couple at 0.0 V. Typical experiments are described.

Scan rate dependence during catalysis: Catalytic waves were obtained for $[Ni(P^{Ph}{}_2N^{pNNA\text{-}SerOMe}{}_2)_2](BF_4)_2$ and $[Ni(P^{Ph}{}_2N^{pNNA\text{-}PheOMe}{}_2)_2](BF_4)_2$ at several acid concentrations at scan rates ranging from 0.1 to 15 $V s^{-1}$ to determine the optimal scan rate at which to collect data. The catalytic activity was independent of scan rate between 1 to 8 $V s^{-1}$, therefore all studies were done using a scan rate of 1 $V s^{-1}$.

Catalysis: In a 4 mL glass vial, 2 mL of a 0.70 mM catalyst solution was made in 0.2 M $Et_4N^+BF_4^-$ acetonitrile solution. A small amount of ferrocene was added as an internal standard and the solution was stirred for 5 min. A voltammogram was measured for the analyte solution at 1 $V s^{-1}$. The analyte solution was then titrated with 20 μL aliquots of 1.0 M $DMFH^+$ in acetonitrile using a 50 μL syringe. The working electrode was polished before each addition of acid and a cyclic voltammogram was measured after each addition of acid. Acid was added to the analyte solution until no further increase in catalytic current was observed (0.08 to 0.11 M $DMFH^+$). Water was then added in 5 μL aliquots using a 10 μL syringe until the catalytic current reached its maximum (~0.70–0.85 M water).

The *meta*- and *para*-substituted non-natural amino acid nickel complexes, $[Ni(P^{Ph}{}_2N^{m/pNNA}{}_2)_2](BF_4)_2$, had different solubility properties in acetonitrile compared to the ester complexes. A typical experiment for catalysis was slightly different for this compound. In a 2 mL glass vial, the catalyst (0.0146 g, 0.01 mmol) was dissolved in acetonitrile (1 mL) and syringe filtered into a clean 2 mL glass vial. To this solution was added $Et_4N^+BF_4^-$ (0.15 g, 0.7 mmol), stirred for 5 min and then syringe filtered into a clean 2 mL glass vial. Then 0.5 mL of this solution was diluted to 1 mL and syringe filtered, this was repeated one more time. The resulting catalyst concentration was approximately 0.5 to 0.7 mM. A small amount of ferrocene was added as an internal standard and the solution was stirred for 5 min. A voltammogram was measured for the analyte solution at 1 $V s^{-1}$. The analyte solution was then titrated with 10 μL aliquots of 1.0 M $DMFH^+$ in acetonitrile using a 50 μL syringe. The working electrode was polished before each addition of acid and a cyclic voltammogram was measured after each addition of acid. Acid was added to the analyte solution until no further increase in catalytic current was observed (0.15 M $DMFH^+$). Water was then added in 2 μL aliquots using a 10 μL syringe until the catalytic current reached its maximum (1.3 M water).

Calculating the rate of H_2 production: The turnover frequency or TOF (k_{obs}, s^{-1}), was calculated from the ratio of the catalytic current (i_{cat}) measured in the acid independent region (Figure S1) to the current obtained for a diffusive one-electron reduction with the catalyst in the absence of acid (i_p), using Equtaion (1):

$$\frac{i_{cat}}{i_P} = \frac{2}{0.4463}\sqrt{\frac{RT \cdot k_{obs}}{Fv}} \quad (1)$$

where R is the gas constant, T is the temperature in Kelvin, F is the Faraday constant, and v is the scan rate ($V s^{-1}$).[21] To determine i_{cat}/i_p, the cathodic current (i_p) was corrected for dilution. The value of i_{cat} was taken where the catalytic current plateaus, where such a plateau was observed, however, all of the *para*-substituted complexes reported here show a nearly constant increase in current with no clear plateau (Figure S5), so i_{cat} was measured at both −0.9 V ($i_{cat\text{-}A}$) and −1.1 V ($i_{cat\text{-}B}$) for all complexes to allow for direct comparison. Each measurement was repeated at least three times for statistical purposes. Overpotentials were calculated using the method of Evans et al. [Eq. (2)],[22] with the $E^\circ_{H^+} = -0.14$ V and the pK_a 6.1.

$$E^\circ_{1/2} = E^\circ_{H^+} - \left(\frac{2.303RT}{F}\right)pK_a \quad (2)$$

Digital simulation of cyclic voltammograms: Kinetic parameters for electron transfer (k_s, $cm s^{-1}$; α) were determined by simulating cyclic voltammograms (CVs) of *m*-NNA-TyrOMe, *p*-NNA-TyrOMe, *m*-NNA-SerOMe, and *p*-NNA-SerOMe, in acetonitrile (0.2 M $Et_4N^+BF_4^-$). For each complex, solutions were prepared with [Ni] = 0.7 mM and [ferrocene] = 0.3 mM. CVs were collected with scan rates of v = 1, 2, 4, 10, 20, and 40 $V s^{-1}$, beginning at a potential positive of the $Ni^{II/I}$ couple, traversing the $Ni^{II/I}$ and $Ni^{I/0}$ couples, and then traversing the $Cp_2Fe^{+/0}$ couple. CVs were referenced to this couple, which was also used to estimate the solution resistance (500 Ω). CVs were truncated after referencing to show only the $Ni^{II/I}$ and $Ni^{I/0}$ couples.

CVs of the electrolyte solution collected using the same parameters as for the complexes were used for background subtraction. The background-subtracted CVs showed unexpected nonzero anodic currents in the initial portion of the cathodic scans, along with a crossing of the cathodic and anodic traces near the turnaround voltage; this was attributed to excess capacitance currents in the background scans. A multiplier m, where $i_{corrected} = i_{observed} - m \times i_{background}$ was refined to minimize the mean squared current $(i_{corrected})^2$ over the first 50 mV of data for each voltammogram. Values determined for m were 0.702–0.835 (*m*-NNA-TyrOMe), 0.670–0.814 (*p*-NNA-TyrOMe), 0.795–0.946 (*m*-NNA-SerOMe), and 0.739–0.882 (*p*-NNA-SerOMe). The background-subtracted data generally showed some residual capacitance; a value of $C_{DL} = 2 \times 10^{-8}$ F was determined by manual adjustment.

The background-subtracted, referenced voltammograms were simulated using DigiElch Version 7.F. Refinement parameters for the $Ni^{II/I}$ and $Ni^{I/0}$ redox couples and for the diffusion coefficients of the Ni species (assumed to be equal for all oxidation states of a given complex) were determined by successive least-squares refinement of calculated versus experimental voltammograms. Initial estimates for the diffusion coefficient D, and for $E°(Ni^{II/I})$ and $E°(Ni^{I/0})$ were obtained using data with v = 1, 2, 4 $V s^{-1}$, assuming $k_s(Ni^{II/I}) = k_s(Ni^{I/0}) = 1$ $cm s^{-1}$. Refinement using all data then afforded estimates of $E°$, α, and k_s for the $Ni^{II/I}$ and $Ni^{I/0}$ couples, and D. For *m*/*p*-NNA-TyrOMe, this refinement converged, with σ = 0.027 and 0.025 for the *meta*- and *para*-substituted complexes. Parameter estimates are provided in Table S3.

Refinement using all data with $E°$, α, and k_s for the $Ni^{II/I}$ and $Ni^{I/0}$ couples and D allowed to vary freely did not converge for *m*/*p*-NNA-SerOMe. Confidence intervals for α and k_s for the $Ni^{I/0}$ couple were much larger than for the $Ni^{II/I}$ couple, and these parameters were taken to be ill-determined. On the assumption that $Ni^{I/0}$ is Nernstian for these complexes, $\alpha(Ni^{I/0})$ was set to 0.5 and $k_s(Ni^{I/0})$ was set to 1 $cm s^{-1}$. Refinement on the remaining parameters converged, with σ = 0.027 and 0.031 for the *meta*- and *para*-substituted complexes. Parameter estimates are provided in Table S4.

Computational methods: Classical molecular dynamics (MD) simulations were carried out using replica-exchange methodology[23] (REMD) to explore the differences in conformational space of the *meta*- and *para*-substituted alanine containing complexes, *m*/*p*-NNA-AlaOEt. The Amber10[24] MD simulation code was used. The force field parameters for the core metal complex, $[Ni(P^{Ph}{}_2N^{Ph}{}_2)_2]^{2+}$, were developed, while the FF99SB[25] force field was used for the ligands. In the $[Ni(P^{Ph}{}_2N^{Ph}{}_2)_2]^{2+}$ moiety, the Ni and P atoms were assigned Blöchl charges,[26] and all other

atoms were given RESP charges.[27] Details about the development of the force field are available in the Supporting Information. The solvent (acetonitrile) was treated implicitly using a modified Generalized Born (GB) model.[28] The REMD simulation utilized 20 replicas and a temperature range of 280.0–930.0 K. The simulations ran for a total of 95 ns, generating ~13000 structures for conformational analysis of the 300 K trajectory.

The interaction of water was also studied by modeling the solvent explicitly in three different systems: *m*/*p*-NN-OEt, *m*/*p*-NNA-AlaOEt, and *m*/*p*-NNA-Lys. Simulations included explicit acetonitrile or acetonitrile/water mixtures representing water concentrations between 0.5 and 3 M. TIP3P water parameters[29] and acetonitrile parameters published by Nikitin and Lyubartsev[30] were used. The modeled systems contained ~900 solvent molecules, with a periodic box of 45 Å × 45 Å × 45 Å for the *m*/*p*-NN-OEt and *m*/*p*-NNA-AlaOEt solutes, and ~3600 solvent molecules in a periodic box of 70 Å × 70 Å × 70 Å for *m*/*p*-NNA-Lys. Statistics were accumulated from ~30 ns trajectories for the *m*/*p*-NN-OEt and *m*/*p*-NNA-AlaOEt, and ~20 ns for *m*/*p*-NNA-Lys, obtained at ambient conditions (pressure of 1 atm and temperature of 300 K). To evaluate the concentration of water molecules near the catalysts, the number of water molecules (N) was counted around the solvent accessible surface as a function of the distance from the surface. The volume (V) around the catalyst was calculated for concentric shells with 1 Å thickness, and the concentration of water was calculated for each shell ($N/V \times N_A$).

The free energy cost was calculated for the structural reorganization of the complexes to allow for direct delivery of protons from the dipeptide to the pendant amine in the catalysts. The simulations used the implicit solvation model and umbrella sampling MD methodology, and the free energy profiles were reconstructed using the WHAM (Weighted Histogram Analysis Method) approach.[31] The umbrella sampling was done in 36 windows, for the *m*/*p*-NNA-Lys system, and 26 windows for *m*/*p*-NNA-AlaOEt, varying the reaction coordinate by 0.5 Å, from 3.0 to 15.5 Å for *m*/*p*-NNA-AlaOEt, and from 3 to 20.5 Å for NNA-Lys. Each trajectory was equilibrated for 500 ps and statistics were collected from 1.5 ns long trajectories. A constraining harmonic potential with a force constant of 20 kcal mol^{-1} was used. Prior to the umbrella sampling, the peptides involved in the dynamics were relaxed using simulated annealing, by gradually heating the system to 800 K then cooling it down and equilibrating at 300 K.

Acknowledgements

The authors would like to thank Dr. Daniel L. Dubois for helpful discussions. This work was funded by the US DOE Basic Energy Sciences, Physical Bioscience program (M.L.R., T.C.S., W.J.S.), the US DOE Basic Energy Sciences, Chemical Sciences, Geoscience and Biosciences Division (A.J., W.J.S.), the Office of Science Early Career Research Program through the Office of Basic Energy Sciences (W.J.S., B.G.P., M.H., S.R.), and the Center for Molecular Electrocatalysis, an Energy Frontier Research Center funded by the US Department of Energy, Office of Science, Office of Basic Energy Sciences (J.A.S.R., S.R.). Part of the research was conducted at the W. R. Wiley Environmental Molecular Sciences Laboratory, a national scientific user facility sponsored by US Department of Energy's Office of Biological and Environmental Research (BER) program located at Pacific Northwest National Laboratory (PNNL). Pacific Northwest National Laboratory is operated by Battelle for the US Department of Energy.

[1] S. Karlin, Z. Zhu, K. Karlin, *Proc Natl. Acad. Sci. USA* **1997**, *94*, 14225–14230.

[2] a) L. Bobadilla, F. Nino, E. Cepeda, M. A. Patarroyo, *Characterizing and predicting catalytic residues in enzyme active sites based on local properties: A machine learning approach* **2007**; b) H. R. Brodkin, W. R. Novak, A. C. Milne, J. A. D′Aquino, N. M. Karabacak, I. G. Goldberg, J. N. Agar, M. S. Payne, G. A. Petsko, M. J. Ondrechen, D. Ringe, *Biochemistry* **2011**, *50*, 4923–4935; c) T. Dudev, Y. L. Lin, M. Dudev, C. Lim, *J. Am. Chem. Soc.* **2003**, *125*, 3168–3180; d) S. Karlin, Z. Y. Zhu, K. D. Karlin, *Biochemistry* **1998**, *37*, 17726–17734; e) C. Yang, X. Li, W. Wei, Y. Li, Z. Duan, J. Zheng, T. Huang, *Chem. Eur. J.* **2007**, *13*, 3120–3130; f) R. Wolfenden, M. J. Snider, *Acc. Chem. Res.* **2001**, *34*, 938–945.

[3] I. V. Korendovych, S. J. Shandler, G. L. Montalvo, W. F. DeGrado, *Org Lett.* **2011**, *13*, 3474–3477.

[4] a) Y. Lu, N. Yeung, N. Sieracki, N. M. Marshall, *Nature* **2009**, *460*, 855–862; b) N. M. Marshall, D. K. Garner, T. D. Wilson, Y.-G. Gao, H. Robinson, M. J. Nilges, Y. Lu, *Nature* **2009**, *462*, 113–116.

[5] a) M. Frey, *ChemBioChem* **2002**, *3*, 153–160; b) C. Léger, A. K. Jones, W. Roseboom, S. P. J. Albracht, F. A. Armstrong, *Biochemistry* **2002**, *41*, 15736–15746; c) A. D. Wilson, R. H. Newell, M. J. McNevin, J. T. Muckerman, M. Rakowski Dubois, D. L. Dubois, *J. Am. Chem. Soc.* **2006**, *128*, 358–366.

[6] a) Y. Nicolet, B. J. Lemon, J. C. Fontecilla-Camps, J. W. Peters, *Trends Biochem. Sci.* **2000**, *25*, 138–143; b) Y. Nicolet, C. Piras, P. Legrand, C. E. Hatchikian, J. C. Fontecilla-Camps, *Structure* **1999**, *7*, 13–23; c) J. W. Peters, W. N. Lanzilotta, B. J. Lemon, L. C. Seefeldt, *Science* **1998**, *282*, 1853–1858.

[7] a) M. L. Helm, M. P. Stewart, R. M. Bullock, M. R. Dubois, D. L. Dubois, *Science* **2011**, *333*, 863–866; b) U. J. Kilgore, J. A. S. Roberts, D. H. Pool, A. M. Appel, M. P. Stewart, M. R. DuBois, W. G. Dougherty, W. S. Kassel, R. M. Bullock, D. L. Dubois, *J. Am. Chem. Soc.* **2011**, *133*, 5861–5872; c) U. J. Kilgore, M. P. Stewart, M. L. Helm, W. G. Dougherty, W. S. Kassel, M. R. DuBois, D. L. Dubois, R. M. Bullock, *Inorg. Chem.* **2011**, *50*, 10908–10918.

[8] A. Volbeda, L. Martin, C. Cavazza, M. Matho, B. W. Faber, W. Roseboom, S. P. Albracht, E. Garcin, M. Rousset, J. C. Fontecilla-Camps, *J. Biol. Inorg. Chem.* **2005**, *10*, 239–249.

[9] T. E. Creighton, *Proteins: Structures and Molecular Properties*, 2nd ed., W. H. Freeman and Company, New York, **1993**.

[10] a) A. Jain, S. Lense, J. C. Linehan, S. Raugei, H. Cho, D. L. Dubois, W. J. Shaw, *Inorg. Chem.* **2011**, *50*, 4073–4085; b) A. Jain, M. L. Reback, M. L. Lindstrom, C. E. Thogerson, M. L. Helm, A. M. Appel, W. J. Shaw, *Inorg. Chem.* **2012**, *51*, 6592–6602.

[11] a) A. El-Faham, F. Albericio, *Chem. Rev.* **2011**, *111*, 6557–6602; b) V. Dourtoglou, J.-C. Ziegler, B. Gross, *Tetrahedron Lett.* **1978**, *19*, 1269–1272; c) R. Knorr, A. Trzeciak, W. Bannwarth, D. Gillessen, *Tetrahedron Lett.* **1989**, *30*, 1927–1930.

[12] I. M. Kolthoff, M. K. Chantooni, S. Bhowmik, *Anal. Chem. (Wash.)* **1967**, *39*, 1627.

[13] A. J. Bard, L. R. Faulkner, *Electrochemical Methods: Fundamentals and Applications*, 2nd ed., Wiley, New York, **2001**.

[14] R. Nicholoson, I. Shain, *Anal. Chem.* **1964**, *36*, 706.

[15] a) The radius of gyration is a measure of the compactness of a molecule, calculated as: $R_g^2 = \frac{1}{n}\sum_{i=1}^{n}(\vec{r}_i - \vec{R}_c)^2$, where $\vec{R}_c$ is the center of geometry of the molecule, $\vec{r}_i$ is the position of atom i, and n is the total number of atoms in the molecule; b) A. Ahmed, F. Rippmann, G. Barnickel, H. A. Gohlke, *J. Chem. Inf. Model.* **2011**, *51*, 1604–1622.

[16] a) J. Lee, N. M. Goodey, *Chem. Rev.* **2011**, *111*, 7595–7624; b) S. W. Ragsdale, *Chem. Rev.* **2006**, *106*, 3317–3337.

[17] K. Izutsu, *Acid–Base Dissociation Constants in Dipolar Aprotic Solvents*, Blackwell Scientific Publications, Oxford, **1990**.

[18] E. S. Wiedner, J. Y. Yang, S. Chen, S. Raugei, W. G. Dougherty, W. S. Kassel, M. L. Helm, R. M. Bullock, M. Rakowski DuBois, D. L. DuBois, *Organometallics* **2012**, *31*, 144–156.

[19] I. Favier, E. Dunach, *Tetrahedron Lett.* **2004**, *45*, 3393–3395.

[20] A. Le Goff, V. Artero, B. Jousselme, P. D. Tran, N. Guillet, R. Metaye, A. Fihri, S. Palacin, M. Fontecave, *Science* **2009**, *326*, 1384–1387.

[21] a) J. M. Savéant, E. Vianello, *Electrochim. Acta* **1965**, *10*, 905–920; b) J. M. Savéant, E. Vianello, *Electrochim. Acta* **1967**, *12*, 629–646; c) D. H. Pool, D. L. DuBois, *J. Organomet. Chem.* **2009**, *694*, 2858–2865.

[22] G. A. N. Felton, R. S. Glass, D. L. Lichtenberger, D. H. Evans, *Inorg. Chem.* **2006**, *45*, 9181–9184.

[23] a) A. Mitsutake, Y. Sugita, Y. Okamoto, *Biopolymers* **2001**, *60*, 96–123; b) H. Nymeyer, S. Gnanakaran, A. E. García, *Meth. Enzymol.*

2004, *383*, 119–149; c) X. Cheng, G. Cui, V. Hornak, C. Simmerling, *J. Phys. Chem. B* **2005**, *109*, 8220–8230.

[24] Amber10, T. A. D. D. A. Case, T. E. Cheatham, III, C. L. Simmerling, J. Wang, R. E. Duke, R. Luo, M. Crowley, R. C. Walker, W. Zhang, K. M. Merz, B. Wang, S. Hayik, A. Roitberg, G. Seabra, I. Kolossváry, K. F. Wong, F. Paesani, J. Vanicek, X. Wu, S. R. Brozell, T. Steinbrecher, H. Gohlke, L. Yang, C. Tan, J. Mongan, V. Hornak, G. Cui, D. H. Mathews, M. G. Seetin, C. Sagui, V. Babin, P. A. Kollman, University of California, San Francisco, **2008**.

[25] P. C. W. D. Cornell, C. I. Bayly, I. R. Gould, K. M. Merz, Jr., D. M. Ferguson, D. C. Spellmeyer, T. Fox, J. W. Caldwell, P. A. Kollman. , *J. Am. Chem. Soc.* **1995**, *117*, 5179–5197.

[26] P. E. Blöchl, *J. Chem. Phys.* **1995**, *103*, 7422–7428.

[27] C. I. Bayly, P. Cieplak, W. Cornell, P. A. Kollman, *J. Phys. Chem. J. Phys. Chem. B* **1993**, *97*, 10269–10280.

[28] A. Onufriev, D. Bashford, D. A. Case, *Proteins Struct. Funct. Bioinf.* **2004**, *55*, 383–394.

[29] W. L. Jorgensen, J. Chandrasekhar, J. Madura, M. L. Klein, *J. Chem. Phys.* **1983**, *79*, 926–935.

[30] A. M. Nikitin, A. P. Lyubartsev, *J. Comput. Chem.* **2007**, *28*, 2020–2026.

[31] S. Kumar, D. Bouzida, R. H. Swendsen, P. A. Kollman, J. M. Rosenberg, *J. Comput. Chem.* **1992**, *13*, 1011–1021.

Received: August 8, 2012
Published online: December 11, 2012

Please note: Minor changes have been made to this manuscript since its publication in *Chemistry—A European Journal* Early View. The Editor.

